

A data-driven analysis of fiber type architecture over the entire muscle

Davide Bindellini

Leids Universitair Medisch Centrum

Lenard M. Voortman

Leids Universitair Medisch Centrum

Cyriel S. Olie

Leids Universitair Medisch Centrum

Maaïke van Putten

Leids Universitair Medisch Centrum

Erik van den Akker

Leids Universitair Medisch Centrum

Vered Raz (✉ v.raz@lumc.nl)

Leids Universitair Medisch Centrum <https://orcid.org/0000-0003-3152-1952>

Methodology

Keywords: quantitative image analysis, muscle architecture, myofiber type, data-driven analysis

Posted Date: May 14th, 2020

DOI: <https://doi.org/10.21203/rs.3.rs-27599/v1>

License:  This work is licensed under a Creative Commons Attribution 4.0 International License.

[Read Full License](#)

Abstract

Background

Skeletal muscle function is inferred from the spatial arrangement of muscle fibers architecture, which corresponds to myofiber molecular and metabolic features. Myofiber types can be distinguished by the expression of myosin heavy chain (MyHC) isoforms, representing contraction properties. In most studies, myofiber typing is determined from a local sampling, typically obtained from the muscle median region. This median region is assumed to represent the entire muscle. However, it remains largely unknown to what extent this local sampling represents the entire muscle.

Methods

We present here a pipeline to study the architecture of muscle fiber type over the entire muscle, from sectioning, staining, imaging to image quantification and data-driven analysis.

Results

We reconstructed muscle architecture from consecutive cross-sections stained for laminin and MyHC isoforms. Examining the entire muscle using consecutive cross-sections is extremely laborious, we provide consideration to reduce dataset and yet to cover the entire muscle. Analyses of over 15,000 myofibers, showed spatial variations in myofiber geometric features, myofiber type and the distribution of neuromuscular junctions along the entire muscle.

Conclusions

We suggest that asymmetric spatial distribution of myofiber types, geometric features of myofibers and the neuromuscular junctions along the muscle could affect muscle function. Therefore, instead of a single sampling from a median region, representative regions covering the entire muscle should be investigated in future studies.

Background

Skeletal muscles facilitate mobilization and stability of the skeleton, which is greatly determined by muscle fiber architecture. Muscle fiber spatial arrangement is broadly described by their orientation relative to the axis of force generation. In general, three main fiber arrangements have been described: 1) fibers arrangement parallel to the force-generating axis on both ends of the muscle. 2) fibers that are oriented at a single angle relative to the force generating axis, and 3) fibers that are oriented at several angles relative to the axis of force generation (Lieber Richard and Ward Samuel, 2011; Lieber and Fridén,

2000; Otten, 1988). It has been recognized that we still far from understand how myofiber properties affect contraction and the specific movement of muscle groups (Herzog, 2017).

In addition, to muscle fiber architecture, contraction properties are also determined by myofiber types. Fast- and slow- twitch muscle fibers can be distinguished by metabolic pathways (Lang et al., 2018; Schiaffino and Reggiani, 2011). Myofibers contractile properties are marked by the expression of myosin heavy chain (MyHC) isoforms (Schiaffino and Reggiani, 2011). The fast-twitch muscle fibers express MyHC-2A, -2B and - 2X isoforms, and slow- twitch express MyHC-1. The MyHC-2B type muscle fibers produce energy by glycolysis, whereas the MyHC-2A type muscle fibers use fatty acids for energy production (Schiaffino and Reggiani, 2011). Myofiber types are also distinguished by molecular networks (Raz et al., 2018). Alterations in MyHC isoform expression occur in physiological conditions like training or aging, and in pathological conditions (Baskin et al., 2015; Pette and Staron, 2000). Understanding alterations in myofiber typing (transitions) in different conditions should employ data-driven (unbiased) analysis of individual myofibers, requiring large myofiber dataset(s).

Methods to stain individual MyHC isoforms using a single antibody mix (Bloemberg and Quadrilatero, 2012; Kammoun et al., 2014), led to the development of image quantification protocols, resulting in large myofiber datasets from which myofiber composition and spatial arrangement could be studied using data-driven analyses (Mayeuf-Louchart et al., 2018; Raz et al., 2019; Y et al., 2020). The high-throughput analysis can further improve understanding of myofiber transitions in disease and physiological conditions (Raz et al., 2019; Riaz et al., 2015; Riaz et al., 2016). Those studies on myofiber composition and changes in disease animal models are most often carried out in cross-sections taken from a median region of the muscle. Yet, it has been reported that the expression of the MyHC isoforms varies over the longitudinal axis of myofibers (Komiya et al., 2017). The spatial organization of myofiber type over the entire muscle is not fully understood.

A simulation of muscle movement has been suggested using architectural models, suggested that even in a muscle with a parallel muscle fiber arrangement, as the tibialis anterior (TA), the contraction is not symmetric along the muscle longitudinal axis (Moo et al., 2016; Moo et al., 2020; Otten, 1988; Van Leeuwen and Spoor, 1992). The tibialis anterior (TA) connects the knee to the foot, mobilizing the lower leg (Mathewson et al., 2012). Modelling of myofiber architecture from non-invasive imaging procedures also reported asymmetric myofiber organization along the TA longitudinal (Damon et al., 2011; Sullivan et al., 2019). These reports demonstrate the importance of analysis of myofibers over the entire muscle. However, they do not discriminate between myofiber types.

We investigated myofiber type arrangement over the entire muscle. We present a pipeline to investigate myofiber architecture using imaging and image quantification over the entire muscle, including essential steps to reduce dataset size. We show an asymmetric distribution of myofiber geometrical features along the muscle and suggest a pattern that could relate to myofiber-typing and the distribution of neuromuscular junctions.

Methods

Mouse and immunohistochemistry procedures

Two TA muscles were excised from two 8-weeks-old male C57BL/6J wild type mice and immediately snap froze in liquid nitrogen in the presence of iso-pentane, as described in (Raz et al., 2019; Riaz et al., 2015). One TA muscle was sectioned in a transverse axis and the other one in a longitudinal axis. Every muscle was sectioned from one end to the other. For each staining, at least three longitudinal sections were used. All 603 transverse sections of 10 μm thick, covering nearly the entire muscle, were stained. The tips at the distal or proximal ends were excluded, as those could not be sectioned. We measured the length of the TA muscle prior to imaging, and it was just over 6 mm (Fig. 1), indicating that sectioning covered nearly the entire muscle. Sections were made with the CM3050-S cryostat (Leica Germany), and were pasted on “PTFE” printed slides, 12 well – 5 mm diameter, (Electron Microscopy Sciences, USA). Sectioning of the entire muscle was carried out in a single session, single day without removing the muscle from the cryotome. This eliminates differences in the cutting angle (tissue orientation, which will affect myofiber geometry) and batch effect. From the TA muscle of the second mouse, longitudinal sections were generated. Muscle sections were stored at $-20\text{ }^{\circ}\text{C}$ prior to staining.

The immunohistochemical procedure was performed with a staining protocol that is detailed in (Raz et al., 2019). Primary antibodies that were used in this study are: Rabbit-anti-Laminin (1:1000, Abcam, UK). Secondary antibodies used are: Goat-anti-Rabbit_Alexa-647 (1:1000, Life Technologies, USA), Goat-anti-Mouse_Alexa-488 (1:1000, Life Technologies, USA). Fluorescently conjugated compounds: antibodies to MyHC-2B_ Alexa fluor-488-conjugated (1:400), MyHC-2A_ Alexa fluor-594-conjugated (1:1000) were homemade (Riaz et al., 2016), and α -Bungarotoxin_Alexa fluor-488-conjugated (1:1000) was purchased from Thermo Fisher. Slides were mounted with ProLong Gold (Invitrogen, USA). The α -Bungarotoxin antibody was used to stain the neuromuscular junction (NMJ). All cross-sections were simultaneously stained using a single antibody mix, in order to eliminate variations between staining sessions.

The length of the entire muscle or individual muscle fibers was measured from longitudinal sections using the microscope scale bar.

Imaging

Imaging was performed with the Panoramic 250 Flash III slide scanner (3DHISTECH, Hungary). Imaging of all cross-sections was carried out in a single session, eliminating batch effects. Imaging of the α -Bungarotoxin signal was performed with both the slide scanner and a higher resolution with the Leica DM5500. The α -Bungarotoxin signal in NMJs was manually counted from digital magnifications of images. Counting was carried out from three sections, by two researchers. The reported counts are an average of two researchers and three sections.

Image processing, quantification and alignment

Slide scanner images were stitched, and files were converted to TIFF using CaseViewer (3DHISTECH, Hungary). After conversion, sections were cropped and scaled using custom MatLab (MathWorks Inc.) scripts. Scaling of the images (down-sampling) was crucial to decrease image size and resolution and thereby to increase the processing speed. All sections were exported at a lower resolution scale. Manual investigation of the images shows broken, folded or poorly mounted sections, which were excluded from further analysis (examples are in Fig. S1). This is expected as all wet lab procedures were carried out manually.

The Tiff images were processed and subsequently were segmented and quantified using the MuscleJ macro in ImageJ (Mayeuf-Louchart et al., 2018). In brief, myofiber objects were identified after segmentation of laminin staining, as reported in (Riaz et al., 2016). An example of tissue outcome is shown in Fig. S2. We applied the following modifications to the original MuscleJ: the image processing step (prior to segmentation) was changed to match our image resolution, implementation of an automatic loading of the whole image set, and an automatic saving of the segmented mask, circularity, the spatial position (X, Y coordinated) was monitored. The output file included: section number, position, myofiber number, CSA, circularity, spatial position, myHC-2B and MYHC-2A mean fluorescence intensity (Table S1). The macro can be obtained upon request. We noticed that this uniform image processing and segmentation settings were not optimal for all sections, but we compromised for a uniform procedure over manual optimization for every section.

We then excluded sections under the following criteria: myofibers were not identified in > 70% of the section area, and gaps between consecutive images are not larger than 150 μm . This step was also beneficial to allow proper componential capacity. In total, from the initial 603 Sect. 150 sections remained for further analysis. Representative segmented images are found in Fig. S3). This step was also beneficial to reduce the dataset size otherwise processing took a few days. The remaining sections were then mapped to their physical position along the muscle longitudinal axis. Section position was calculated with the first section at zero μm and consecutively increasing by 10 μm (sections thickness), including the position of the excluded sections. Median and variance for both cross-sectional area (CSA) and circularity were calculated per section. MyHC mean fluorescence intensity (MFI) was obtained after background correction that was separately applied to each image and each fluorophore, as described in (Riaz et al., 2016). Additionally, a '2A mask' was generated marking the 2A-positive fibers, which were added onto the laminin-segmentation mask. Fibers were considered 2A-positive when their MFI was greater than the MFI mean + one standard deviation of all the fibers per section.

The alignment of the images was performed with the '2A masks' in ImageJ using Linear Stack Alignment with the scale-invariant feature transformation (SIFT) algorithm (Lowe, 2004). This method aligns sections consecutively one by one.

Myofiber composition analysis was carried out using R (version 3.5.1). In total, 153930 fibers were obtained from the eligible 150 cross-sections and were used in the data-driven analysis. In order to reduce technical differences between images, MFI values were scaled per section. Scaling of myofiber dataset

has been demonstrated to be beneficial for myofiber type data-driven analysis (Y et al., 2020). Data-driven analysis of myofibers was carried out after a natural logarithm (ln) transformation of MFI values. Smoothing lines were calculated and plotted using the smooth.spline function in R, using smoothing parameter = 1. Statistical significance was assessed with Pearson's chi-squared test.

Results

To develop a methodology reconstructing the 3D-architecture of myofiber type over the entire muscle, we selected the TA of a wild type mouse for its small, which is suitable for such an initial study. The workflow of this methodology is summarized in Fig. 1. One muscle was cross sectioned from the proximal to the distal end, and the other one was sectioned on the longitudinal axis. The entire muscle length was measured to be around 6 mm (Fig. 2B and 2C), which is in agreement with the TA length that was reported in (Heemskerk et al., 2005) Image processing and quantification were carried out on the cross-sections, and data-driven analyses were carried out on data generated from cross-sections. The longitudinal sections were used as reference for coordinates and verifications of results from the cross-sections. A schematic representation of the TA anatomy is shown in Fig. 2A. The muscle fiber (named here as myofiber) contours were stained with an anti-laminin antibody, and myofiber types were recognized with an antibody mix to MyHC-2A and MyHC-2B (Fig. 2C and 2D). Both MyHC isoforms are commonly used for myofiber typing in mouse (Bloemberg and Quadrilatero, 2012). MyHC-2A expression in TA is found in only a subset of muscle fibers (Raz et al., 2019; Riaz et al., 2015). Throughout the entire muscle, muscle fibers positive to MyHC-2B were more prominent compared with MyHC-2A, and some MyHC-2B myofibers encompassed the entire muscle length (Fig. 2C). The length of MyHC-2A myofibers was estimated from three longitudinal sections, (ranged between 160–250 μm), which was used as a criterion for section exclusion.

The wet-lab and imaging steps: cryo-sectioning, immunostaining and imaging were completed within a single batch to avoid technical variations. Sectioning the entire muscle in a single day, without removing the mounted muscle from the machine, ensured that the section angle did not change throughout the entire muscle. Together, this procedure minimizes technical variation that could give rise to potential confounding batch effects. Imaging was carried out in a single batch using a slide scanner, all slides were imaged using the same settings. From all acquired images myofibers were segmented based on the lamina staining using single image processing and image quantification procedures. To assess this protocol, the results of lamina segmentation were manually compared to the original images. We noticed that the quality of part of the sections was not sufficient for further processing, either due to technical issues (sectioning or folded/broken tissue sections) or bad segmentation. Those sections were excluded under the general guideline for data reduction, allowing a gap of maximum 150 μm between two consecutive sections. This gap size was smaller than the estimated shortest myofiber length (160 μm). With this criterion we ensured that all myofibers in the muscle tissue will be included in subsequent analyses. In addition, this gap distance was kept constant along the muscle to avoid a bias for over- or under- representative areas.

To investigate changes in myofiber spatial organization along the longitudinal axis we aligned the cross-sections using the laminin-based segmentation and MyHC-2A positive fibers (Fig. 2E). The MyHC-2A myofibers were defined as positive when the mean fluorescence intensity (MFI) was greater than mean MFI + one standard deviation per section. Reconstruction of muscle fiber architecture along the longitudinal axis was carried out with the SIFT algorithm. A good alignment was found for consecutive sections over a short distance (AVI. S1). However, the alignment over a larger distance required compromising with reduced dataset for a faster solution. The alignment outcomes that were obtained with gaps between sections were comparable to the alignment without gaps in the same region (AVI. S2, AVI S1, respectively). Since the alignment procedure only accounted for consecutive sections, consecutive alignment of pairs of sections (local) was hampered by the accumulation of errors over sets of sections. Therefore, alignment over the entire muscle was performed in parts. We obtained good alignment results from both proximal and median regions of the muscle, whereas alignments of sections at the distal region were poor (Fig. S1). A good alignment over distance can result from a parallel orientation of muscle fibers. A poor alignment over a small distance could indicate bending of the muscle or a not-parallel orientation of muscle fibers.

The change in myofiber alignment along the longitudinal axis suggests that myofiber properties might alter over the entire muscle. To investigate this, we considered only cross sections with good segmentation (> 85% of the sections were eligible based on segmentation). In total, 153,930 objects from 150 cross-sections were included in the analysis (the full dataset is found in Table S1). From the laminin segmented objects, representing myofiber objects, we extracted cross-sectional area (CSA) and circularity. As the entire muscle was sectioned in a single session, the same cutting angle was kept along the entire muscle, therefore a change in CSA or circularity could not reflect alterations in sectioning orientation but can indicate a biological phenomenon. From each cross section we calculated the median CSA, mean circularity and the variance of both features. A smoothed regression line (curved), which levels off small variations between adjunct cross sections, was applied to assess the change along the entire muscle (Fig. 3). The smoothed regression line enables considering major changes along the longitudinal axis, while disregarding the effect of an individual cross-section or a small group of consecutive sections. The shape of the regression line for the number of myofibers follows the macro shape of the TA muscle: smallest at the proximal end, large at the median part followed by smaller size at the distal end (Fig. 3A). At the central region we noticed few groups of consecutive sections with distinguished numbers of myofibers (Fig. 3A, 2500–3500 μm), since those did not influence the regression line, they were not considered here. The median CSA plot showed two main regions, in sections at the first $\sim 1/3$ rd of the muscle the median CSA was smaller than the other part of the muscle. The regression line showed a constant CSA along the other $2/3$ rd part of the muscle (Fig. 2B). The regression line of the mean circularity showed a similar trend as median CSA along the muscle (Fig. 3C). However, the variance of circularity showed an opposite trend along the muscle (Fig. 3C). At the proximal end the circularity median was low, indicating an elongated orientation of the myofibers, and high variance, indicating heterogeneity. In contrast, at distal and median regions variance in circularity was low and median circularity was high (Fig. 3C). In contrast, the changes in median and variance CSA along the muscle were

similar (Fig. S4). Using the intersection between the mean circularity regression line and the circularity variance regression line we defined the proximal end (Fig. 3C). We then superimposed the CSA and circularity curves in order to assess a spatial relation between these two geometrical features. The intersection between the regression defined the distal end sub-region (Fig. 3D). Together, the features sub-regions can be summarised as follows (see also in Fig. 3F): the proximal end (< 1/9 of the muscle) myofibers CSA is small and circularity is low with high variance indicating heterogeneity in myofiber structure. Consequently, in region I (< 1/9 of the muscle) circularity increases but myofiber CSA remains small. Then after, in the median part (~ 5/9th of the muscle length), myofibers have high CSA and circularity values. The small variance in circularity suggests a more homogenous structure of fibers. At the distal end, the relations between circularity and CSA were inverse as compared with the preceding region (Fig. 3D). This region is also the one with poor alignment (Fig. S1).

We then investigated if these muscle regions, as defined by geometrical features of myofibers, can be distinguished by molecular features of muscle biology. We focus on the sarcomeric proteins, MyHC-2B and MyHC-2A, and the distribution of NMJs. The cross-sections were stained with antibody mix to MyHC isoforms, and after imaging the MFI were measured from each myofiber. Main myofiber-type subclasses were determined in the pooled dataset using density plots. The MyHC-2B density plot showed only a single peak, indicating a predominant one myofiber type (Fig. S5A), but two peaks were found in the MyHC-2A density plot (Fig. S5B). This indicated that in TA two myofiber populations are found with high and low MyHC expression, whereas the MyHC-2B myofibers can be described as a homogenous population. For a quantitative assessment of the distribution of the MyHC-2A myofibers along the muscle, we discriminated between the MyHC-2A positive myofibers and the MyHC-2A negative myofibers using density distribution of myHC-2A MFI (Fig. S5B). We then calculated the percentage of 2A-positive myofibers in every section (Fig. 3E). Overall, the regression line of the proportions of the 2A-positive myofibers is consistent with that of the median CSA, the proportions of 2A-positive myofibers were higher at the proximal region, compared with median and distal regions (Fig. 3E). Interestingly, a significant difference of MyHC-2A positive myofibers was found between the percentages of the 2A-positive fibres in each muscle region ($p\text{-value} < 2.2 \times 10^{-16}$). The asymmetric distribution of MyHC-2A myofibers along the longitudinal axis suggests that contraction properties are not uniform along the muscle.

Last, we investigated the distribution of NMJs along the muscles and visually assessed a relation to muscle regions. The NMJs were visualized in three longitudinal sections with α -bungarotoxin, which specifically binds to NMJs (Tse et al., 2014). A representative image is shown in (Fig. S6). The four muscle regions were estimated from the cross-sectional study, using the scale of the muscle longitudinal axis. In this muscle, neuromuscular junctions were absent at the proximal-end region and were rare at the distal end (Fig. 3F). The majority of NMJs (85%) were counted in the median region of the muscle (Fig. 3F).

Discussion

The impact of myofiber type on muscle physiology and function has been mostly interpreted from cross sections at the median part of the muscle. Several reports reinforced the importance to sample the entire muscle in order to understand how myofiber architecture affects muscle function (Moo et al., 2020; Stark and Schilling, 2010). In contrast to previous studies (Dickinson et al., 2018; Heemskerk et al., 2005; Moo et al., 2020; Nyakatura et al., 2019; Stark and Schilling, 2010), we also considered the spatial organization of myofiber types over the entire muscle. Our methodological paper, therefore, also reinforces the importance of adequate spatial sampling of whole muscles in future studies.

Modelling muscle fiber architecture has been studied using non-invasive methods and ex-vivo imaging procedures. For the mouse TA a parallel myofiber arrangement has been reported, where most fibers are parallel to the longitudinal axis at the largest part of the muscle, but close to the tendon at the proximal and distal ends myofibers curve (Heemskerk et al., 2005; Lovering et al., 2013; Moo et al., 2016). This indicates an asymmetric myofiber architecture along the muscle. Ex-vivo measurements of sarcomere force-length demonstrated that the muscle fiber architecture affects its biomechanical properties (Moo et al., 2020). Ex-vivo procedures of muscle architecture can influence the shape of the muscle during the following procedures: 1. pulling when dissecting the muscle out of the mouse. We were careful avoiding pulling tissue, yet this can influence when comparing between different muscles. 2. As the muscle is not connected to the tendon, the natural muscle-tendon tension cannot be considered. This can affect the muscle tension and length, but how fast this muscle-tendon tension is lost is not well unknown. But a fast tissue freezing, immediately after muscle harvesting, we expect to reduce this loss of tissue tension and length. However, freezing artefacts could also contribute to variations between muscle tissues. 3. Mounting would affect myofiber orientation. Therefore, in our workflow sectioning of the entire muscle was carried out in a single day, without dismounting of the muscle from the cryotome, and the section angle relative to the muscle axis was identical across all sections. Despite those all possible effects, our observations using ex-vivo analysis of myofiber organization over the entire murine TA muscle are in agreement with the in vivo studies. We also found asymmetric myofiber arrangement along the longitudinal axis, and between proximal and distal regions. At the proximal end myofibers were parallel to the longitudinal axis, but at the distal end myofiber orientation was altered, suggesting bending. Ideally, an ex-vivo study of myofiber architecture would be performed in sections of an entire lower leg, in which a muscle is connected to the bone(s) and other tissues exactly as in the full organism. This approach could be investigated in future studies, making use of the workflow we are reporting here.

The distribution of myofiber types along the entire muscle was also previously reported (Wang et al., 2002), but this is the first study combining immunofluorescence of MyHC isoforms and data-driven analysis. Compared with the ATPase-based analysis of myofiber typing, image analysis of MyHC immunofluorescence can be applied for image quantification and more robust downstream analysis of myofiber typing (Mayeuf-Louchart et al., 2018). Furthermore, the four most abundant MyHC isoforms can be investigated in a single study (Riaz et al., 2016; Y et al., 2020). Using ATPase staining, an asymmetric distribution slow-twitch muscle fibers was found in rat limb muscles, including the TA (Wang et al., 2002). Here we also report asymmetric myofiber distribution along the murine TA muscle. The MyHC-2B positive myofibers seem to stretch over the entire muscle length, but the MyHC-2A positive myofibers are more

abundant in the proximal part of the muscle. The other two MyHC isoforms that are often considered in mouse muscle fiber typing are MyHC-1 and MyHC-2X (Rao and Mohanty, 2019; Riaz et al., 2016). We excluded MyHC-1 in the antibody mix, as its expression in TA muscle is limited. We also excluded the MyHC-2X as imaging with the Panoramic 250 Flash III slide scanner was not optimal for 4 fluorophores. Both MyHC-2B and -2A isoforms indicate different metabolic processes, their asymmetric distribution may suggest differences in contraction properties along the muscle. We could not conclude whether the MyHC-2B myofibers at the distal end are the curved counterparts of the myofibers seen in the median part of the muscles.

In contrast to most studies that determine myofiber typing from a single region (often median), this study investigates the distribution of myofiber typing along the entire muscle. However, including all cross sections covering the entire muscle is highly laborious and requires an enormous computational power. Here we show that using the shortest myofiber length as a guideline for gaps between consecutive cross-sections enabled us to eliminate proportions of the cross-sections without losing spatial information. Since we show here that myofiber typing changes along the muscle, it potentially implicates that disease- and age-associated alterations in myofiber type composition could be more affected in specific muscle regions.

Analytical two-dimensional skeletal muscle models predicted that fibers' shape affect intramuscular pressure distribution (van Leeuwen and Spoor, 1996). Other models suggest that pressure distribution along the muscle is not even, the high-pressure region presents half-way along the muscle length, which supports bending of the muscle fibres (Van Leeuwen and Spoor, 1992). At the centre of the TA muscle we found that both CSA and circularity have the largest range. This could indicate that the geometry of those myofibers support high pressure. The opposite myofiber geometry was found at the proximal end. The small CSA and circularity could indicate that the proximal end of the TA is a vulnerable area for muscle pressure. The observed asymmetry of geometrical features of myofibers along the entire muscle is consistent with biomechanical models of the TA muscle (Heemskerk et al., 2005; Lovering et al., 2013; Moo et al., 2016). Moo et al., also measured sarcomere force at the median region of a muscle and stressed that their findings may not be valid to other muscle regions, especially where myofiber lengths in not uniform (Moo et al., 2020). Under the assumption that we aim to describe major changes along the muscle, we applied a smoothed regression line to describe changes in myofiber features along the muscle. In this analysis, we discarded changes in CSA and myofiber numbers were found in only a small number of sections at the median part of the muscle. Combining the regression lines of CSA and circularity we described four muscle regions and suggest a relation with MyHC-2A positive myofibers and the NMJs: the largest muscle part, the median region (region II) is characterized by high circularity and high CSA, less MyHC-2A positive myofibers and higher density of NMJs. The shortest regions are the proximal and distal ends. Both differ in the orientation of myofibers (varied circularity), the percentage of MyHC-2A positive myofibers, and have the lowest proportions of NJMs. Based on circularity, myofibers at the proximal end are more heterogeneous compared to those at the distal end. The second sub-region (region I), could be a transition region between proximal and median regions. It was reported that higher NMJs concentration implicated higher contraction (Lomo, 2003), suggesting that in the TA the signal is

mainly found at the median part of the muscle. Yet, our observations were made from a single muscle and conclusions should be cautiously made.

Conclusion

In this methodological paper we describe a pipeline to investigate myofibers features along the entire muscle. Based on geometrical features of myofibers we show asymmetric distribution and a spatial pattern along the muscle and distinguish between four main regions. The distribution of myofiber types and NMJs along the muscle agrees with that of myofiber geometrical features, suggesting an asymmetric myofiber contraction along the muscle, which can play a role in muscle physiology and pathological conditions.

Abbreviations

Cross sectional area

CSA

Mean fluorescence intensity

MFI

Myosin heavy chain

MyHC

Natural logarithm

ln

Neuromuscular junction

NMJ

Scale-invariant feature transformation

SIFT

Tibialis anterior

TA

Declarations

- Ethics approval and consent to participate -not applicable.
- Consent for publication -not applicable.
- Availability of data and materials -All scripts are available upon request. The Myofiber dataset that was used in this study is available in Table S1.
- Competing interests - All authors have no conflict of interests on the submission form.
- Funding –the French Muscular Dystrophy Association #26110 to VR.
- Authors' contributions -, Wetlab experiments were performed by DB and CSO; imaging, image processing and image analysis were performed by DB and LMV; muscles were collected by MvP;

project supervision was carried out by LMV, EvdA and VR; funding was received for VR; All authors read and approved the final manuscript.

- Acknowledgements -not applicable.

References

1. Baskin KK, Winders BR, Olson EN. Muscle as a "mediator" of systemic metabolism. *Cell Metab.* 2015;21:237–48.
2. Bloemberg D, Quadriatero J. Rapid determination of myosin heavy chain expression in rat, mouse, and human skeletal muscle using multicolor immunofluorescence analysis. *PLoS One.* 2012;7:e35273–3.
3. Damon BM, Buck AKW, Ding Z. Diffusion-Tensor MRI Based Skeletal Muscle Fiber Tracking. *Imaging Med.* 2011;3:675–87.
4. Dickinson E, Stark H, Kupczik K. (2018). Non-Destructive Determination of Muscle Architectural Variables Through the Use of DiceCT. *Anatomical record (Hoboken, NJ: 2007)* 301, 363–377.
5. Heemskerk AM, Strijkers GJ, Vilanova A, Drost MR, Nicolay K. Determination of mouse skeletal muscle architecture using three-dimensional diffusion tensor imaging. *Magnetic resonance in medicine.* 2005;53:1333–40.
6. Herzog W. Skeletal muscle mechanics: questions, problems and possible solutions. *Journal of NeuroEngineering Rehabilitation.* 2017;14:98.
7. Kammoun M, Cassar-Malek I, Meunier B, Picard B. A simplified immunohistochemical classification of skeletal muscle fibres in mouse. *Eur J Histochem.* 2014;58:2254–4.
8. Komiya Y, Sawano S, Mashima D, Ichitsubo R, Nakamura M, Tatsumi R, Ikeuchi Y, Mizunoya W. Mouse soleus (slow) muscle shows greater intramyocellular lipid droplet accumulation than EDL (fast) muscle: fiber type-specific analysis. *J Muscle Res Cell Motil.* 2017;38:163–73.
9. Lang F, Khaghani S, Türk C, Wiederstein JL, Hölper S, Piller T, Nogara L, Blaauw B, Günther S, Müller S, et al. Single Muscle Fiber Proteomics Reveals Distinct Protein Changes in Slow and Fast Fibers during Muscle Atrophy. *J Proteome Res.* 2018;17:3333–47.
10. Lieber Richard L, Samuel W, R. Skeletal muscle design to meet functional demands. *Philosophical Transactions of the Royal Society B: Biological Sciences.* 2011;366:1466–76.
11. Lieber RL, Fridén J. Functional and clinical significance of skeletal muscle architecture. *Muscle Nerve.* 2000;23:1647–66.
12. Lomo T. What controls the position, number, size, and distribution of neuromuscular junctions on rat muscle fibers? *J Neurocytol.* 2003;32:835–48.
13. Lovering RM, Shah SB, Pratt SJP, Gong W, Chen Y. Architecture of healthy and dystrophic muscles detected by optical coherence tomography. *Muscle Nerve.* 2013;47:588–90.
14. Lowe DG. Distinctive Image Features from Scale-Invariant Keypoints. *Int J Comput Vision.* 2004;60:91–110.

15. Mathewson MA, Chapman MA, Hentzen ER, Fridén J, Lieber RL. Anatomical, architectural, and biochemical diversity of the murine forelimb muscles. *J Anat.* 2012;221:443–51.
16. Mayeuf-Louchart A, Hardy D, Thorel Q, Roux P, Gueniot L, Briand D, Mazeraud A, Bougle A, Shorte SL, Staels B, et al (2018). MuscleJ: a high-content analysis method to study skeletal muscle with a new Fiji tool. *Skeletal muscle* 8, 25.
17. Moo EK, Fortuna R, Sibole S, Abusara Z, Herzog W. (2016). In vivo Sarcomere Lengths and Sarcomere Elongations Are Not Uniform across an Intact Muscle. *Frontiers in Physiology* 7.
18. Moo EK, Leonard TR, Herzog W. (2020). The sarcomere force-length relationship in an intact muscle-tendon unit. *The Journal of experimental biology* 223.
19. Nyakatura JA, Baumgarten R, Baum D, Stark H, Youlatos D. Muscle internal structure revealed by contrast-enhanced μ CT and fibre recognition: The hindlimb extensors of an arboreal and a fossorial squirrel. *Mammalian Biology.* 2019;99:71–80.
20. Otten E. Concepts and models of functional architecture in skeletal muscle. *Exerc Sport Sci Rev.* 1988;16:89–137.
21. Pette D, Staron RS. Myosin isoforms, muscle fiber types, and transitions. *Microscopy research technique.* 2000;50:500–9.
22. Rao VV, Mohanty A. (2019). Immunohistochemical Identification of Muscle Fiber Types in Mice Tibialis Anterior Sections. *Bio-protocol* 9, e3400.
23. Raz V, Raz Y, Vijver Dvd, Bindellini D, Putten Mv, Akker EB.v.d. (2019). High-throughput data-driven analysis of myofiber composition reveals muscle-specific disease and age-associated patterns. *FASEB J* 33, 4046–53.
24. Raz V, Riaz M, Tatum Z, Kielbasa SM, Hoen PACT. The distinct transcriptomes of slow and fast adult muscles are delineated by noncoding RNAs. *FASEB J.* 2018;32:1579–90.
25. Riaz M, Raz Y, Moloney EB, van Putten M, Krom YD, van der Maarel SM, Verhaagen J, Raz V. (2015). Differential myofiber-type transduction preference of adeno-associated virus serotypes 6 and 9. *Skeletal muscle* 5, 37–37.
26. Riaz M, Raz Y, van Putten M, Paniagua-Soriano G, Krom YD, Florea BI, Raz V. PABPN1-Dependent mRNA Processing Induces Muscle Wasting. *PLoS Genet.* 2016;12:e1006031.
27. Schiaffino S, Reggiani C. Fiber types in mammalian skeletal muscles. *Physiological reviews.* 2011;91:1447–531.
28. Stark H, Schilling N. A novel method of studying fascicle architecture in relaxed and contracted muscles. *J Biomech.* 2010;43:2897–903.
29. Sullivan SP, McGeachie FR, Middleton KM, Holliday CM. (2019). 3D Muscle Architecture of the Pectoral Muscles of European Starling (*Sturnus vulgaris*). *Integrative Organismal Biology* 1.
30. Tse N, Morsch M, Ghazanfari N, Cole L, Visvanathan A, Leamey C, Phillips WD. (2014). The neuromuscular junction: measuring synapse size, fragmentation and changes in synaptic protein density using confocal fluorescence microscopy. *J Vis Exp,* 52220.

31. Van Leeuwen JL, Spoor CW. Modelling mechanically stable muscle architectures. *Philosophical Transactions of the Royal Society of London Series B: Biological Sciences*. 1992;336:275–92.
32. van Leeuwen JL, Spoor CW. A two dimensional model for the prediction of muscle shape and intramuscular pressure. *Eur J Morphol*. 1996;34:25–30.
33. Wang L, Copray S, Brouwer N, Meek MF, Kernell D. Regional distribution of slow-twitch muscle fibers after reinnervation in adult rat hindlimb muscles. *Muscle Nerve*. 2002;25:805–15.
34. Y R, EB, v.d.A., T, R., M, R., O, v.d.R., HED, S., N, L., SA, S., M, v.P., EJM, F., *et al.* (2020). A data-driven methodology reveals novel myofiber clusters in older human muscles. *FASEB journal: official publication of the Federation of American Societies for Experimental Biology* *In Press*.

Figures

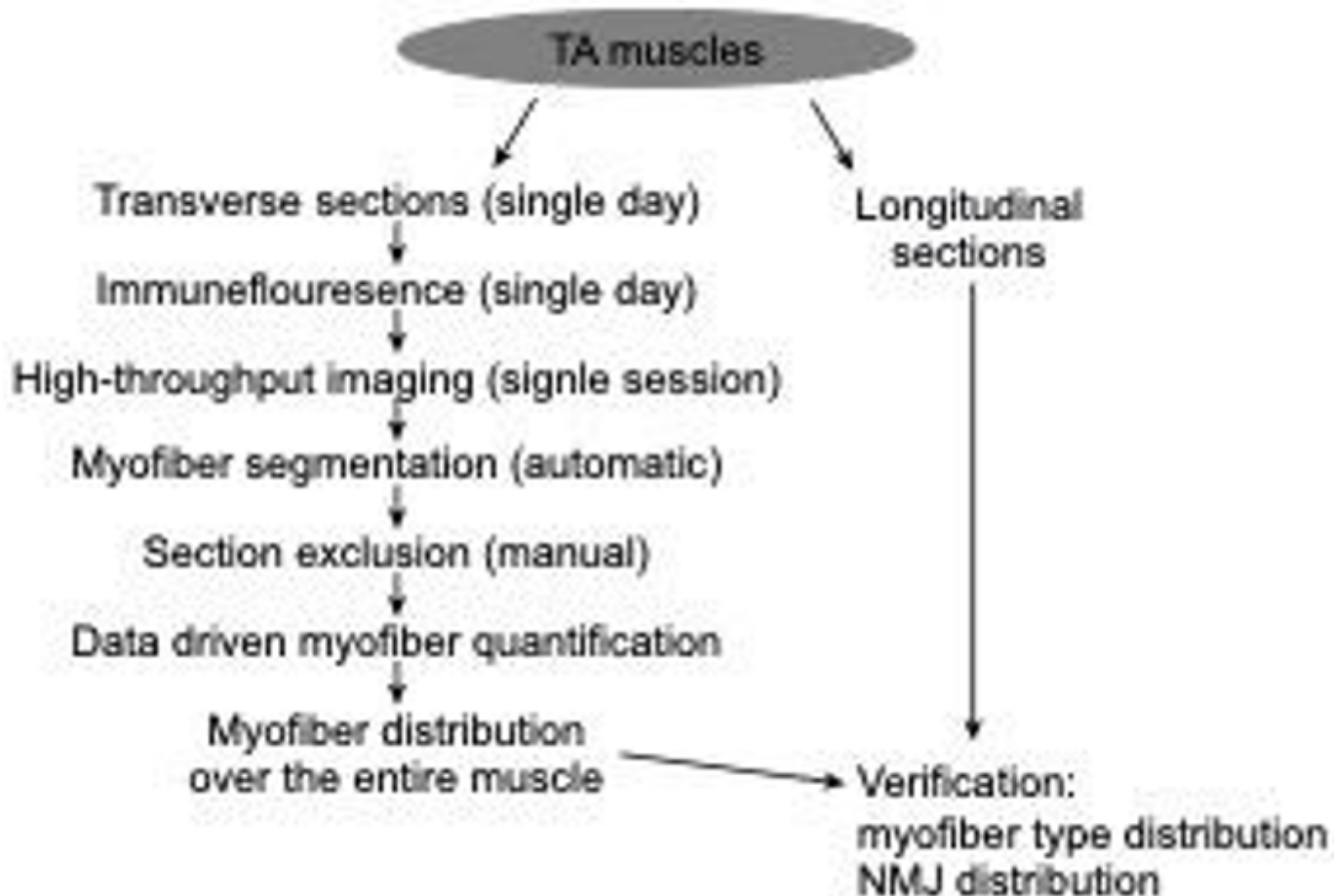


Figure 1

A methodological summary of myofiber data collection and analysis. The workflow of the transverse sections is shown at the left side. The steps from sectioning to imaging were carried out stimulatingly (in

brackets) for all sections to avoid technical differences between sections. Exclusion of sections was based on the segmentation step and it was a manual step. The asymmetric distribution of myofibers and expression of markers were verified in the longitudinal sections.

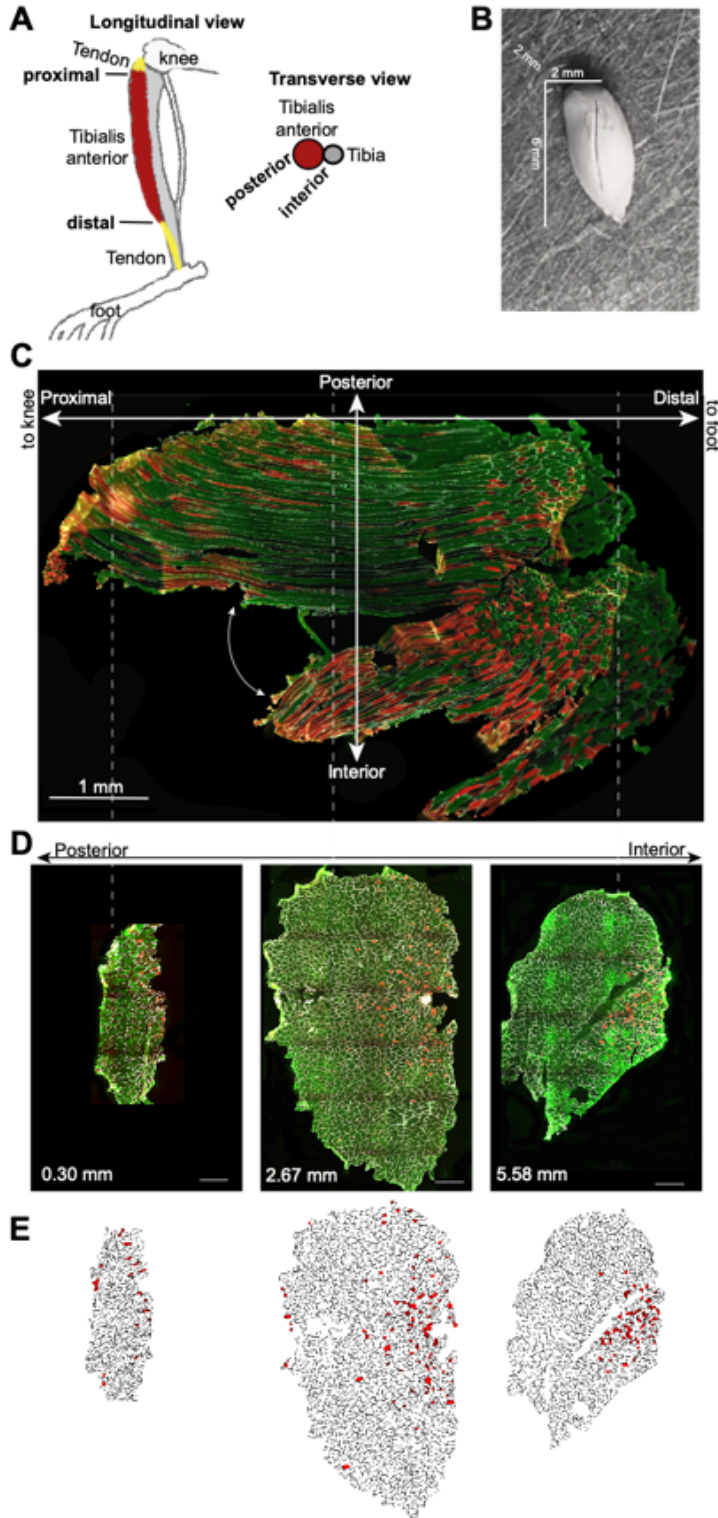


Figure 2

A summary of Tibialis anterior imaging A) A schematic representation of the tibialis anterior anatomy in a longitudinal and transverse views. The tibia is depicted in dark grey, the TA muscle in dark red and the

tendon in yellow. B) An image of a TA muscle prior to sectioning. Sectioning was carried out along the longitudinal line. C) An immunofluorescence image of a longitudinal section from a TA muscle. Muscle positions are as in panel A. Scale bar is 1mm. Dashed white lines are estimated to proximal, median and distal regions, and correspond to the localization cross-sections in D. The curved white arrow depicts the area that detached during sectioning. D) Immunofluorescence images of cross-sections. The position of each cross section is depicted in the bottom left corner, and the dashed lines marker the corresponding position in the longitudinal section. Cross-section orientation (Posterior – interior) is marked. Scale bar is 0.1mm. E) Laminin segmentation of the cross-sections shown in D, with the MyHC-2A positive myofibers depicted in red. Immunofluorescence in C and D were carried out for Laminin (in white), MyHC-2A (in red), and MyHC-2B (in green).

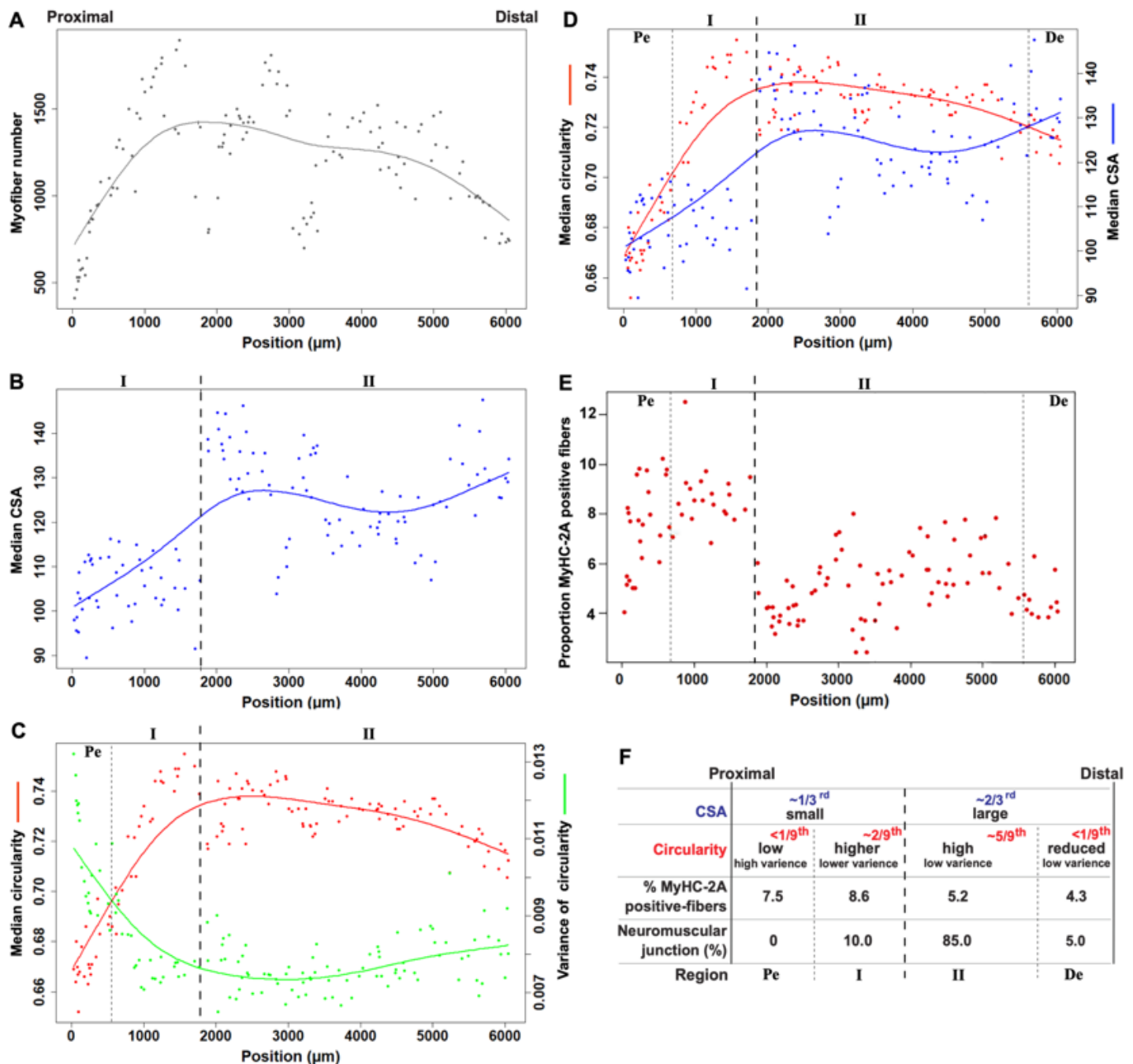


Figure 3

Spatial changes along the TA muscle A-E) Scatter plots of measurements from each cross-section across the entire muscle. Every dot represents a cross-section. Cross-sections are positioned in a chronological order from the proximal to distal end (x-axis, in μm). A smoothed regression line (curved line) is depicted. The A vertical dashed line shows muscle regions (I and II), the and dotted lines the proximal or distal ends (Pe and De, respectively). A. Number of myofibers per tissue cross-section area. B. Median of fiber CSA per section. Regions I and II are distinguished by the median CSA. C. Fiber circularity per section, mean (in red) and variance of the mean (in green). The proximal end (Pe) is defined by the intersection between mean circularity and variance of circularity. Regions I and II are projected from B. D. Mean circularity (in red) and median CSA (in blue). The distal end (De) is defined by the intersection between mean circularity and median CSA. Regions I and II are projected from B, and Pe from C. E. Proportion of MyHC-2A positive fibers. The muscle regions, Pe, I, II and De are projected from E. F. A summary of features per muscle region. Muscle regions that are based on the CSA are depicted in blue, and these based on circularity are in red. % of MyHC-2A positive-fibers were calculated from total fibers. % NMJ is calculated from total NMJ over the entire muscle. The muscle regions, Pe, I, II and De are projected from E.

Supplementary Files

This is a list of supplementary files associated with this preprint. Click to download.

- [AnimationS2.avi](#)
- [TableS1.csv](#)
- [AnimationS1.avi](#)
- [Supplementarymaterial.pdf](#)